

<https://doi.org/10.1038/s41535-025-00767-2>

Pressure-induced structural phase transitions in CrSBr



Luther J. Langston¹, Alberto M. Ruiz², Carla Boix-Constant², Samuel Mañas-Valero², Eugenio Coronado², José J. Baldoví², Zhenxian Liu³ & Janice L. Musfeldt^{1,4}✉

There is growing interest in combining chemical complexity with external stimuli like pressure, field, and light for property control in van der Waals solids. This is because extreme conditions trigger the development of new states of matter and functionality. In this work, we bring together synchrotron-based infrared absorption, Raman scattering, and diamond anvil cell techniques with first-principles calculations of the lattice dynamics and energy landscape to reveal the series of structural phase transitions in CrSBr. By tracking how the phonons change under pressure, we uncover a remarkable chain of complex symmetry modifications, interlayer interactions, and chemical reactions. A group-subgroup analysis suggests that CrSBr undergoes an orthorhombic $Pmmn \rightarrow$ monoclinic $P2_1/m$ transition at 7.6 GPa, and based upon a comparison with model oxychlorides like FeOCl and CrOCl, we propose that changes in the pendant halide groups drive the system to a $P2_1/m$ -like space group above 15.3 GPa. Compression above 20.2 GPa is irreversible, resulting in the formation of an entirely new compound that is metastable for months. This work opens the door to the use of pressure and possibly strain to control the properties of CrSBr.

van der Waals solids are legendary for their complex energy landscapes, sensitivity to external stimuli, and property control through chemical substitution. Amongst the various external stimuli, such as magnetic field, strain, and light, pressure is a potent tool for tuning properties because it acts directly on bond lengths and angles, controls the c/a ratio, and modifies the van der Waals gap^{1–5}. In transition metal dichalcogenides like MoS₂ and WS₂, work has focused on pressure-driven insulator-to-metal transitions, interactions between superconductivity and competing states, and the mechanisms of solid-state lubrication^{6–9}. There are many exciting high-pressure properties and states of matter in the MPX₃ family of materials ($M = \text{Fe, Cr, Mn, Co, Ni}$, and $X = \text{S, Se}$) as well¹⁰. Significantly less is known about other van der Waals solids under compression. While efforts have been made to reveal the phase diagrams of magnetic insulators like CrSiTe₃, CrI₃, and Mn₃Si₂Te₆^{11–13}, van der Waals magnets such as CrSBr^{14–16} have received markedly less attention, which is surprising since CrSBr is reported to be air stable. This system is a metamagnet, formed by anisotropic ferromagnetic layers coupled antiferromagnetically to one another, exhibiting antiferromagnetic ordering below 133 K, a direct bandgap of 1.5 eV, and spin-mediated exciton-phonon coupling^{17–24}. CrSBr exfoliates easily, and van der Waals heterostructures of this material have been used in magnetic tunnel junctions and spin valves, offering a route toward atomically thin memory devices^{23,24}. Despite many promising discoveries in the few- and single-layer limit^{25–35}, understanding how external stimuli like pressure

impacts the properties of this class of materials is highly under-explored. To our knowledge, there has been only a single study on the impact of chemical and physical pressure on the magnetic properties of CrSBr³⁶. While chemical pressure in the form of Cl substitution for Br drives a crossover in anti-ferromagnetic to ferromagnetic coupling, compression systematically reduces the Néel temperature, smoothly evolves the lattice parameters, and modifies the exchange interactions due to local structure changes in the 0–1.9 GPa range³⁶. These early results suggest that still greater pressures could trigger even more interesting magnetic and excitonic behavior³⁶ as well as other highly advantageous processes.

In this work, we combined diamond anvil cell techniques and synchrotron-based infrared absorption and Raman scattering with a group-subgroup symmetry analysis, lattice dynamics calculations, and an analysis of the energy landscape to reveal the properties of CrSBr under pressure. From an examination of the phonon behavior under compression, we identify a series of structural phase transitions at 7.6, 15.3, and 20.2 GPa associated with a remarkable chain of symmetry modifications, interlayer interactions, and chemical reactions. For instance, at $P_{C,1} = 7.6$ GPa, we find a continuous volume change accompanied by a significant modification of the infrared pattern which, when combined with a group-subgroup analysis, is consistent with an orthorhombic $Pmmn$ to monoclinic $P2_1/m$ transition. $P_{C,2}$ is the pendant halide transition, akin to what is observed in FeOCl^{37–39}. By contrast, $P_{C,3}$ functions as an irreversibility limit which, when surpassed,

¹Department of Chemistry, University of Tennessee, Knoxville, TN, USA. ²Instituto de Ciencia Molecular, Universitat de Valencia, Paterna, Spain. ³Department of Physics, University of Illinois, Chicago, IL, USA. ⁴Department of Physics and Astronomy, University of Tennessee, Knoxville, TN, USA. ✉e-mail: musfeldt@utk.edu

triggers a chemical reaction in this system upon pressure release. The resulting state is metastable for months, offering an interesting platform for additional investigation. These results highlight the rich behavior of CrSBr under pressure and the potential for compression (and presumably strain) to control properties for future applications^{40,41}.

Results and discussion

Ambient pressure vibrational properties of CrSBr

Figure 1 displays the infrared spectrum of CrSBr at ambient conditions. Group theory predicts a total of six infrared-active vibrational modes for an orthorhombic material with the $Pmmn$ space group: $2B_{1u} + 2B_{2u} + 2B_{3u}$ ²⁰. This is precisely what we find, although the broad band between 300 and 350 cm^{-1} must be fit with model oscillators to resolve the individual peaks. An example of this deconvolution process is shown in Supplementary Note 4. Vibrational mode assignments were made using our complementary lattice dynamics calculations. The details are summarized in Table 1. For instance, we describe the motion of the B_{2u} mode at 92 cm^{-1} as shearing of the outer Br atoms against the inner CrS bilayer. The high frequency modes are various types of Cr–S stretches.

Figure 2 displays the Raman scattering response of CrSBr at ambient conditions. There are three strong peaks at 114, 245, and 343 cm^{-1} . These features are assigned as 1A_g , 2A_g , and 3A_g phonons, in excellent agreement with our lattice dynamics calculations [Table 1]. Each manifests varying degrees of interlayer character, exhibiting motion along the stacking direction. The lowest frequency 1A_g mode consists of bromine atoms vibrating toward adjacent layers, whereas the high frequency 3A_g mode shows intralayer character along the c -axis primarily involving the inner CrS bilayer with suppressed Br motion⁴². B_g symmetry features are also allowed in the Raman scattering response^{42,43}, although they are extremely weak. Similar behavior is seen in other layered materials^{37,39,44}.

Structural phase transitions in CrSBr under pressure

Figure 3 summarizes the infrared properties of CrSBr under pressure. All six phonons harden under compression, a normal trend for a material in a diamond anvil cell⁴⁵. The $^1B_{2u}$ mode is weak and disappears near 7 GPa. Figure 3b focuses on the behavior of the $^1B_{3u}$ and $^1B_{1u}$ modes at 179 and 225 cm^{-1} . While the $^1B_{1u}$ peak diminishes and eventually disappears, the $^1B_{3u}$ peak appears to split into a doublet near 15 GPa, although this “splitting” is actually new peak activation. The third panel summarizes the

response of the broad band, which, as discussed previously, can be deconvoluted into three separate features using standard peak-fitting techniques. These phonon modes become more distinct under compression because their frequencies harden at different rates. The $^2B_{3u}$ mode moves systematically under compression, indicating that the symmetry element it represents is unperturbed. The $^2B_{2u}$ mode also hardens with only modest changes in its overall trend. The behavior near the high-frequency $^2B_{1u}$ mode is the most interesting. A new peak appears above 7.5 GPa and again at approximately 20 GPa. These changes are quite dramatic and signal strong symmetry breaking with the activation of new modes due to the development of lower symmetry phases under pressure.

We combine these trends to generate the frequency versus pressure plot shown in Fig. 3d. The mode trends define three critical pressures, separating four structural phases, including the $Pmmn$ phase at ambient

Table 1 | Phonon modes of CrSBr related to this work

Mode	Theory (cm^{-1})	Experiment (cm^{-1})	Mode description
Infrared			
$^1B_{2u}$	89.4	91.6	In-plane shearing of Br centers against the CrS double layer
$^1B_{3u}$	162.6	179.8	In-plane shearing of Br centers against the CrS double layer
$^1B_{1u}$	215.3	225.9	Out-of-plane, out-of-phase stretching of Br against CrS
$^2B_{3u}$	301.3	312.9	In-plane, out-of-phase stretch of Cr against S
$^2B_{2u}$	302.1	329.1	In-plane, out-of-phase motion of Cr against S
$^2B_{1u}$	340.5	350.6	Out-of-plane, out-of-phase stretch of Cr against S
Raman			
1A_g	125.9	114.1	Out-of-plane motion of Br and Cr centers against neighbors
2A_g	246.1	244.9	Out-of-plane motion of CrS dimers against the neighbors
3A_g	328.5	343.4	Out-of-plane motion of a CrS layer against the other

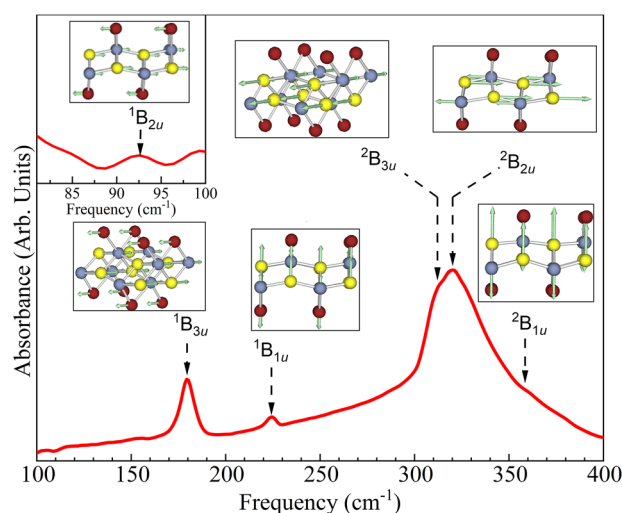


Fig. 1 | Infrared absorbance of CrSBr. Synchrotron infrared spectrum of CrSBr at ambient conditions and the theoretically calculated mode displacement patterns. Blue, yellow, and red represent chromium, sulfur, and bromine atoms, respectively. The inset shows a close-up view of the weak $^1B_{2u}$ phonon with its displacement pattern. The positions of the $^2B_{3u}$, $^2B_{2u}$, and $^2B_{1u}$ modes were determined using traditional oscillator fitting techniques as discussed in the text.

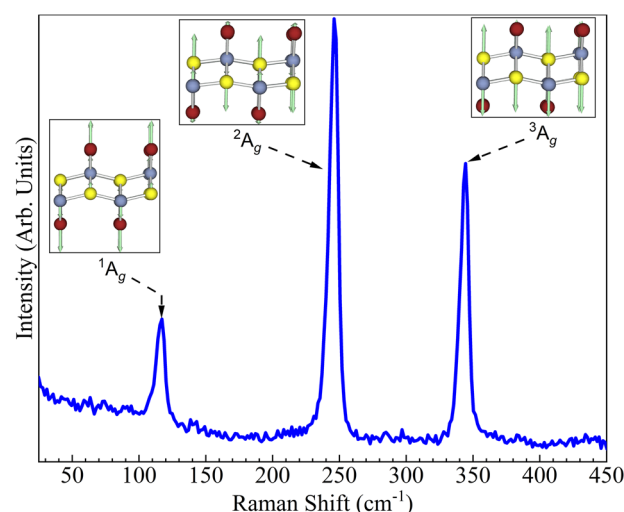


Fig. 2 | Raman-active vibrational modes in CrSBr. Raman scattering spectrum of CrSBr taken near ambient conditions inside the diamond anvil cell along with our theoretically calculated mode displacement patterns. The three Raman-active A_g modes are easily identified. The B_g symmetry modes are not clearly observed here⁴³.

Fig. 3 | Infrared response of CrSBr under pressure. **a–c** Close-up views of the infrared spectra under compression. The phonon mode symmetries are labeled. **d** Frequency versus pressure trends as a function of pressure. $P_{C,1}$, $P_{C,2}$, and $P_{C,3}$ denote the critical pressures separating ambient and high-pressure phases.

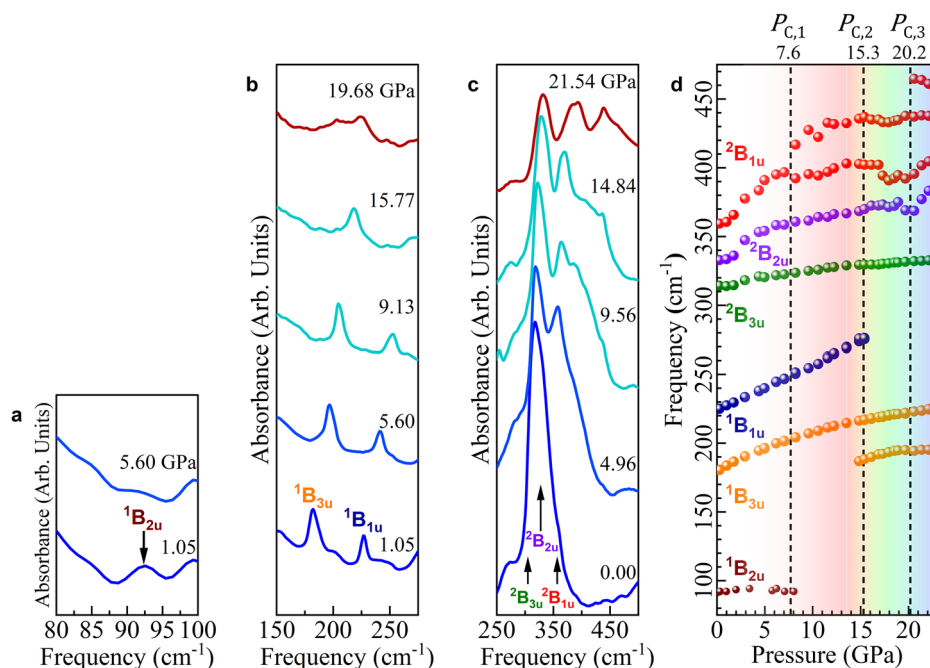
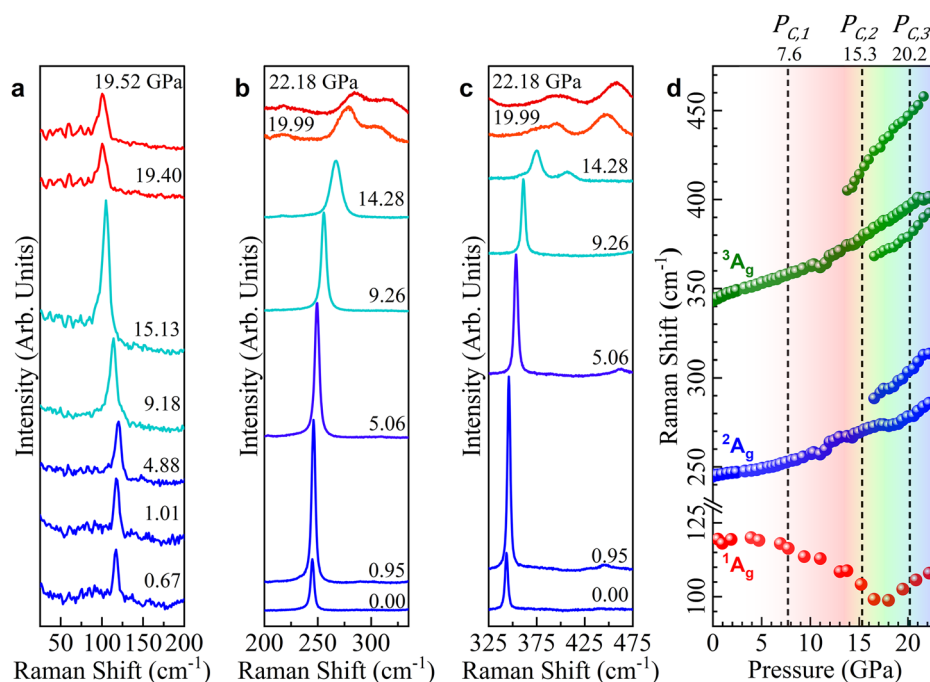


Fig. 4 | Raman scattering response of CrSBr under pressure. **a–c** Close-up views of the Raman-active 1A_g , 2A_g , and 3A_g modes. The phonon mode symmetries are labeled. **d** Summary of the frequency versus pressure trends for the Raman-active vibrational modes in CrSBr. The critical pressures are indicated.



conditions. We find $P_{C,1} = 7.6$ GPa. It is defined by the disappearance of the $^1B_{2u}$ mode and the development of a new peak near the high-frequency $^2B_{1u}$ phonon. $P_{C,2}$, the second critical pressure, presents itself at approximately 15.3 GPa and is evidenced by the disappearance of the $^1B_{1u}$ phonon mode and the appearance of the peak near 175 cm⁻¹. The additional peak that develops near the high-frequency $^2B_{1u}$ mode defines $P_{C,3}$ at approximately 20 GPa. Since various peaks appear and disappear, we know that CrSBr has both symmetry restorations and reductions under pressure. We can use these spectral changes to reveal the symmetry behavior of the high-pressure phases. Even though the phonon modes differ, six infrared modes are active in the ambient pressure phase and across $P_{C,1}$ and $P_{C,2}$. The highest pressure

phase above $P_{C,3}$ has a total of seven infrared-active modes, indicating an overall decrease in the symmetry. No evidence of metallicity is observed even up to 50 GPa. This is different than many other complex chalcogenides that host insulator-to-metal transitions under pressure¹⁰.

Figure 4 summarizes the Raman scattering response of CrSBr under compression. The most dramatic effect is that while the 2A_g and 3A_g modes harden under pressure, the 1A_g phonon softens overall. Typical mechanisms for mode softening include phase transitions, electron-phonon coupling, temperature changes, doping, and hydrogen bonding, among others^{46–48}, although the situation is different here. As discussed below, we attribute the 1A_g mode softening to buckling of the pendant halide groups. Figure 4a

Table 2 | Group-subgroup pathways for CrSBr across $P_{C,1}$ and the corresponding infrared- and Raman-active modes

Path	Sequence across $P_{C,1}$	Γ_{optic}	
		IR Active	Raman Active
1	$Pmmn^{(59)} \xrightarrow{\text{Down}} Pmm2^{(25)} \xrightarrow{\text{Up}} Cmm2^{(35)}$ $Imm2^{(44)}$	$2A_1 + 2B_1 + 2B_2$ $2A_1 + 2B_1 + 2B_2$	$2A_1 + 2B_1 + 2B_2$ $2A_1 + 2B_1 + 2B_2$
2	$Pmmn^{(59)} \xrightarrow{\text{Down}} Pmn2_1^{(31)} \xrightarrow{\text{Up}} Amm2^{(38)}$ $Imm2^{(44)}$	$2A_1 + 2B_1 + 2B_2$ $2A_1 + 2B_1 + 2B_2$	$2A_1 + 2B_1 + 2B_2$ $2A_1 + 2B_1 + 2B_2$
3	$Pmmn^{(59)} \xrightarrow{\text{Down}} P2_1/m^{(11)} \xrightarrow{\text{Up}} P2/m^{(10)}$	$2A_u + 4B_u$	$4A_g + 2B_g$
4	$Pmmn^{(59)} \xrightarrow{\text{Down}} P2_12_12^{(18)} \xrightarrow{\text{Up}} C222^{(21)}$ $I222^{(23)}$	$2B_1 + 2B_2 + 2B_3$ $2B_1 + 2B_2 + 2B_3$	$2B_1 + 2B_2 + 2B_3$ $2B_1 + 2B_2 + 2B_3$
5	$Pmmn^{(59)} \xrightarrow{\text{Up}} Cmmm^{(65)} \xrightarrow{\text{Down}} Cmm2^{(35)}$ $Amm2^{(38)}$	$2B_1 + 2B_2 + 2B_3$ $2A_1 + 2B_1 + 2B_2$ $2A_1 + 2B_1 + 2B_2$	$2B_1 + 2B_2 + 2B_3$ $2A_1 + 2B_1 + 2B_2$ $2A_1 + 2B_1 + 2B_2$
6	$Pmmn^{(59)} \xrightarrow{\text{Up}} Imm^{(71)} \xrightarrow{\text{Down}} Imm2^{(44)}$ $I222^{(23)}$	$2A_1 + 2B_1 + 2B_2$ $2A_1 + 2B_1 + 2B_2$	$2A_1 + 2B_1 + 2B_2$ $2A_1 + 2B_1 + 2B_2$

highlights these trends. There is a slight hardening of the 1A_g mode up to approximately 5 GPa, above which the peak softens considerably with each consecutive pressure step until about 15 GPa, after which it hardens again. As a reminder, this mode is extremely sensitive to out-of-plane Br motion. The phonon softening and peak activation in the Raman scattering response is consistent with the series of structural distortions and three critical pressures established above. Figure 4d summarizes the frequency versus pressure trends for the Raman-active modes. Again, we observe the same critical pressures of 7.6, 15.3, and 20.2 GPa. Notice that $P_{C,1}$ coincides with the pressure at which the 1A_g mode begins to soften.

Symmetry analysis across the structural phase transition at 7.6 GPa

We employed the Bilbao Crystallographic Server as a tool to unravel the symmetry progression across $P_{C,1}$ from the orthorhombic $Pmmn$ phase of CrSBr at ambient conditions to a new space group above $P_{C,1}$ ⁴⁹. We used group-subgroup relations (based on Landau's theory of phase transitions) to determine potential space groups associated with the symmetry changes. This approach is successful because the irreducible representations of distinct crystal phases exhibit the full crystal symmetry^{50,51}. Many candidate space groups and pathways were evaluated based on the following caveats. Due to the inherent nature of the space groups containing translational symmetry elements, the order in which these symmetry changes may very well result in different sets of space groups, so we evaluated all reasonable possibilities. The mode progression across $P_{C,1}$ contains symmetry restoration and symmetry breaking [Figs. 3 and 4]. Therefore, the first step is to realize that all subgroups and supergroups related to the ambient pressure phase must be evaluated to provide a thorough understanding of which structure ultimately results. Table 2 shows several simplified candidate pathways for $P_{C,1}$. Focusing first on the infrared-active modes, we recall that the $^1B_{2u}$ mode disappears near 7.6 GPa, whereas a new feature appears at 420 cm^{-1} alongside the $^2B_{1u}$ mode. All Raman-active modes harden on approach to $P_{C,1}$. The 1A_g mode softens dramatically after the transition is complete, although there is no change in the number of features. The other key finding is that six infrared-active modes are present in the ambient pressure phase and six in the high-pressure phase. There is no change in the number of A_g modes within our sensitivity, so the symmetry operations that correspond to these modes are unchanged. Furthermore, none of the spectral features overlap [Fig. S5, Supplementary Note 6], meaning that the rule of mutual exclusion is active. This implies that inversion symmetry is not broken, so we can eliminate polar space groups from consideration. Additional detail is available in Supplementary Note 6. The space groups assumed in each step of the symmetry analysis were further refined such that the symmetry elements of each subgroup must also be present in the parent group to have a viable pathway between one another. These vibrational mode patterns are distinct for each phase of CrSBr.

Table 2 summarizes the results of our analysis. We show several different subgroup and supergroup pathways, the subsequent space

group, and the predicted number of vibrational modes for that space group. Using the Bilbao Crystallographic Server, we also calculated the different infrared- and Raman-active modes for the resulting space group(s) of each pathway. Several stringent criteria help us refine the results in Table 2. Most importantly, we require six infrared-active phonons and *at least* three Raman-active phonons in the high-pressure phase. We also require an inversion center (due to the rule of mutual exclusion). With these candidate pathways, it is easy to realize that the only viable path is orthorhombic $Pmmn$ to monoclinic $P2_1/m$ across $P_{C,1}$. The other pathways do not agree with the experimental spectra because their phonon modes would require the same activity in both infrared absorbance and Raman scattering, which is not the case given our observations.

Structure-property relations in chalcogen-halides

Materials structurally and chemically similar to CrSBr, such as FeOCl and CrOCl, underscore common mechanisms of pressure-induced structural phase transitions. Like CrSBr, FeOCl, and CrOCl host ambient pressure orthorhombic $Pmmn$ space groups with transition metal chalcogen bilayers sandwiched between layers of dangling halides that act to create the van der Waals gap⁵². Single-crystal X-ray diffraction within a diamond anvil cell reveals that FeOCl displays a $Pmmn$ to monoclinic $B2_1/m$ phase transition near 15 GPa³⁷. The latter is the same as $P2_1/m$ but with a different primary axis. CrOCl also displays a $Pmmn$ to incommensurate phase transition near 16 GPa³⁸. Transitions in these materials are attributed to the buckling of the halide centers as they rearrange to accommodate denser packing upon compression^{37,38}. After the buckling occurs, the monoclinic angle for the oxy-halides^{37,38} is on the order of 90.015° . Raman scattering corroborates these findings in FeOCl, highlighting significant spectral changes across the 15 GPa critical pressure³⁷. Two new modes emerge as the van der Waals gap narrows and the lattice distorts, leading to a buckling of the halide layers³⁷.

Figure 5 displays the Raman scattering response of CrSBr and FeOCl. Some of the spectral features in FeOCl were not present in ref. 37. Even so, a direct comparison is striking. Both materials display pressure-driven structural phase transitions near 15 GPa, and based upon the prior mechanistic work by Bykov et al. on FeOCl³⁷, the transition in CrSBr is likely due to halide buckling driven by the need to maintain favorable halide-halide distances. That said, the vibrational pattern of the oxy-halide is not a perfect match with that of CrSBr, suggesting that the space group may only be $P2_1/m$ -like due to the large number of possible buckling configurations. Considering the similarity between these two materials, it may be worthwhile to use infrared techniques to search for a lower-pressure transition in FeOCl. Other oxy-halides like TiOBr and TiOCl host $P2_1/m$ phases as well³⁹. Even so, we emphasize that CrSBr hosts three critical pressures. Only $P_{C,2}$ where the halide buckling occurs, is mechanistically similar. The other steps in the sequence are unique.

Pressure cycling drives an irreversible structural phase transition in CrSBr

It is well known that pressure cycling can be used to develop new materials^{51,53–55}. In the case of CrSBr, vibrational spectroscopy reveals an additional structural phase transition upon decompression. Figure 6 summarizes the spectroscopic response of CrSBr upon compression to 22 GPa and subsequent release. The released form of the material differs from that of

the starting compound. New phonon modes appear in the infrared absorption and Raman scattering spectra at approximately 12 GPa when the sample is decompressed from pressures above $P_{C,3}$. These features are maintained when the sample is fully released. At this time, we do not know much about this new phase except that it has lower symmetry than $Pmmn$ (with both in- and out-of-plane symmetry breaking) and is stable, lasting for at least ten months at ambient pressure outside of the diamond anvil cell. It is therefore amenable to additional investigation. As noted by Pawbake et al., minor changes in the light incidence angle or slight sample tilting at extreme pressures can give rise to angular-dependent phonon modes, such as the B_g modes observed after compressing past $P_{C,3}$ ⁴³. However, even when accounting for these features, additional vibrational modes emerge in samples compressed beyond the third critical pressure [Fig. S6, Supplementary Note 7]. Interestingly, we can only access this pathway from pressures higher than $P_{C,3}$ [Fig. S6, Supplementary Note 7]. Cycling to $P_{C,2}$ or $P_{C,1}$ does not drive this structural phase transition. This reinforces the existence of $P_{C,3}$ and provides a route to interesting new functionality that is very much path dependent.

Methods

Crystal growth and loading of the diamond anvil cell

Single crystals of CrSBr were synthesized using a modified chemical vapor transport method discussed previously^{14,17,22,56,57}. A small piece was placed in a symmetric diamond anvil cell. The diamond anvil cell was equipped with synthetic type II-a diamonds with 300 μm culets⁵⁸. A stainless steel gasket was pre-indented to a thickness of 48 μm ; the hole size was 150 μm . The pressure-transmitting medium was petroleum jelly and KBr for infrared and Raman scattering measurements, respectively, to achieve a quasi-hydrostatic environment. An annealed ruby ball was employed to determine pressure⁵⁹. As shown in Fig. S1 of Supplementary Note 1, the ruby fluorescence is symmetric with well-separated R1 and R2 lines over the full pressure range of our work.

Spectroscopic measurements

The vibrational properties of CrSBr were investigated using synchrotron infrared and Raman scattering spectroscopies. High-pressure synchrotron infrared measurements were performed using the 22-IR-2 beamline at the

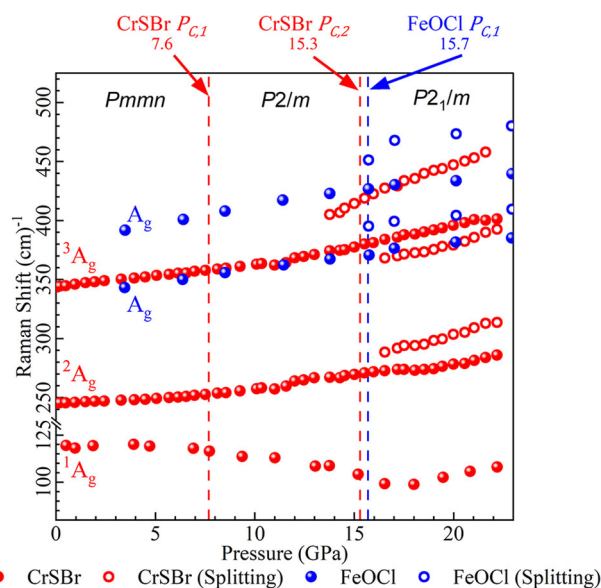


Fig. 5 | Raman scattering response of CrSBr and FeOCl as a function of pressure. Frequency versus pressure plots of the Raman-active modes of CrSBr and FeOCl at room temperature. All Raman modes of FeOCl were digitized directly from Bykov et al.³⁷. The vertical dashed lines denote the critical pressures for each material. Space groups are indicated. The 15 GPa buckling transition is seen in both materials, and it appears to lead to a $P2_1/m$ -like space group in CrSBr.

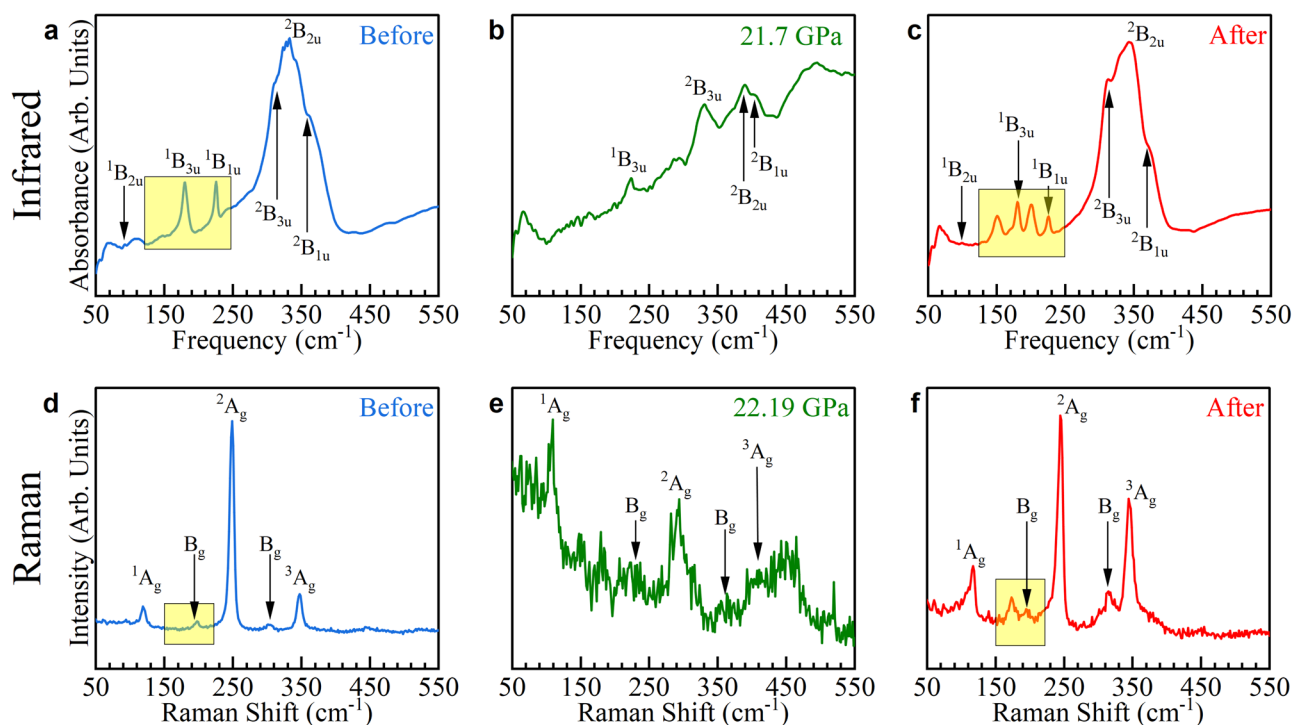


Fig. 6 | Symmetry breaking due to pressure cycling. Infrared and Raman spectra of CrSBr taken before sample compression (a, d) at 22 GPa (b, e) and after (c, f) pressure release. Yellow boxes highlight comparative differences.

National Synchrotron Light Source II (NSLS-II) at Brookhaven National Laboratory. The infrared spectra were collected in the far-infrared range (50–700 cm^{-1} ; 4 cm^{-1} resolution; transmission geometry) using a Bruker 80v equipped with a helium-cooled bolometer. The sample thickness must be carefully chosen to control optical density. Raman scattering spectra were measured with a Horiba Lab RAM spectrometer, a 532 nm excitation laser, a 100 \times working distance objective, 1800 line/mm gratings, and a cold CCD detector. Each scan was 60 s and averaged appropriately. Measurements focused on the 0–25 GPa pressure range at room temperature. Pressure was determined by ruby fluorescence [Fig. S1, Supplementary Note 1].

Symmetry analysis

The structural phase transition of CrSBr across the first critical pressure was analyzed using group-subgroup relations. The Bilbao Crystallographic Server was employed to identify the possible space group symmetries based on the number of changes in phonon modes^{60–63}. The analysis involved plotting the phonon mode frequencies as a function of pressure and identifying the symmetry elements associated with each phase transition via the appearance and disappearances of phonon modes at specific pressures.

First-principles calculations

Frequencies, symmetries, and mode displacement patterns were obtained using first-principles spin-polarized density functional theory (DFT) calculations in the plane wave formalism as implemented in the Quantum ESPRESSO package⁶⁴. The exchange-correlation energy is calculated using the generalized gradient approximation (GGA) using the Perdew–Burke–Ernzerhof (PBE)⁶⁵ functional and standard Ultra-soft (USPP) solid-state pseudopotentials extracted from the Materials Cloud Database. The electronic wave functions were expanded with well-converged kinetic energy cut-offs for the wave functions (charge density) of 50 (400). The crystal structures were fully optimized using the Broyden–Fletcher–Goldfarb–Shanno (BFGS) algorithm until the forces on each atom were smaller than 1×10^{-4} Ry/au and the energy difference between two consecutive relaxation steps was less than 1×10^{-5} Ry. Grimme-D2 dispersion corrections were added to account for van der Waals interactions between adjacent layers. The Brillouin zone was sampled by a fine Γ -centered $8 \times 8 \times 6$ k-point Monkhorst-Pack⁶⁶. The phonon spectrum was calculated using a $3 \times 3 \times 2$ supercell employing the Phonopy code⁶⁷.

Data availability

Data are available from the corresponding authors upon reasonable request.

Received: 22 November 2024; Accepted: 24 April 2025;

Published online: 11 June 2025

References

- Grochala, W., Hoffmann, R., Feng, J. & Ashcroft, N. W. The chemical imagination at work in very tight places. *Angew. Chem. Int. Ed.* **46**, 3620–3642 (2007).
- Xiao, J.-R., Yang, S.-H., Feng, F., Xue, H.-G. & Guo, S.-P. A review of the structural chemistry and physical properties of metal chalcogenide halides. *Coord. Chem. Rev.* **347**, 23–47 (2017).
- Xu, K., Miao, X. & Xu, M. The structure of phase-change chalcogenides and their high-pressure behavior. *Phys. Status Solidi RRL* **13**, 1800506 (2019).
- Zhang, L., Wang, Y., Lv, J. & Ma, Y. Materials discovery at high pressures. *Nat. Rev. Mater.* **2**, 1–16 (2017).
- Pei, S., Wang, Z. & Xia, J. High pressure studies of 2d materials and heterostructures: a review. *Mater. Des.* **213**, 110363 (2022).
- Chi, Z.-H. et al. Pressure-induced metallization of molybdenum disulfide. *Phys. Rev. Lett.* **113**, 036802 (2014).
- Nayak, A. P. et al. Pressure-induced semiconducting to metallic transition in multilayered molybdenum disulphide. *Nat. Commun.* **5**, 1–9 (2014).
- Park, S. et al. Superconductivity emerging from a stripe charge order in IrTe_2 nanoflakes. *Nat. Commun.* **12**, 3157 (2021).
- O’Neal, K. R. et al. High pressure vibrational properties of WS_2 nanotubes. *Nano Lett.* **16**, 993–999 (2016).
- Matsuoka, T., Kim, H.-S., Samanta, S., Musfeldt, J. L. & Mandrus, D. G. MPX_3 van der Waals magnets under pressure ($M = \text{Mn, Ni, V, Fe, Co, Cd}$; $X = \text{S, Se}$). *Front. Mater.* **11**, 1362744 (2024).
- Ghosh, A. et al. Exotic magnetic and electronic properties of layered CrI_3 single crystals under high pressure. *Phys. Rev. B* **105**, L081104 (2022).
- Olmos, R. et al. Pressure-dependent magnetic properties of quasi-2d $\text{Cr}_2\text{Si}_2\text{Te}_6$ and $\text{Mn}_3\text{Si}_2\text{Te}_6$. *J. Phys. Chem. C* **127**, 10324–10331 (2023).
- Musfeldt, J. L., Mandrus, D. G. & Liu, Z. Insulator–metal transition in CrSiTe_3 triggered by structural distortion under pressure. *npj 2D Mater. Appl.* **7**, 28 (2023).
- Beck, J. Über chalcogenidhalogenide des chroms synthese, kristallstruktur und magnetismus von chromsulfidbromid, CrSBr. *Z. Anorg. Allg. Chem.* **585**, 157–167 (1990).
- Göser, O., Paul, W. & Kahle, H. Magnetic properties of CrSBr. *J. Magn. Magn. Mater.* **92**, 129–136 (1990).
- Tabataba-Vakili, F. et al. Doping-control of excitons and magnetism in few-layer CrSBr. *Nat. Commun.* **15**, 4735 (2024).
- Telford, E. J. et al. Layered antiferromagnetism induces large negative magnetoresistance in the van der Waals semiconductor CrSBr. *Adv. Mater.* **32**, 2003240 (2020).
- Klein, J. et al. The bulk van der Waals layered magnet CrSBr is a quasi-1d material. *ACS Nano* **17**, 5316–5328 (2023).
- Lin, K. et al. Strong exciton–phonon coupling as a fingerprint of magnetic ordering in van der Waals layered CrSBr. *ACS Nano* **18**, 2898–2905 (2024).
- Uykur, E. et al. Phonon and magnon dynamics across antiferromagnetic transition in 2d layered van der Waals material CrSBr. Preprint at <https://arxiv.org/abs/2405.07853v1> (2024).
- Watson, M. D. et al. Giant exchange splitting in the electronic structure of a-type 2d antiferromagnet CrSBr. *npj 2D Mater. Appl.* **8**, 54 (2024).
- Boix-Constant, C. et al. Probing the spin dimensionality in single-layer CrSBr van der Waals heterostructures by magneto-transport measurements. *Adv. Mater.* **34**, 2204940 (2022).
- Boix-Constant, C. et al. Multistep magnetization switching in orthogonally twisted ferromagnetic monolayers. *Nat. Mater.* **23**, 212–218 (2024).
- Chen, Y. et al. Twist-assisted all-antiferromagnetic tunnel junction in the atomic limit. *Nature* **632**, 1–7 (2024).
- Esteras, D. L., Rybakov, A., Ruiz, A. M. & Baldoví, J. J. Magnon straintronics in the 2D van der Waals ferromagnet CrSBr from first-principles. *Nano Lett.* **22**, 8771–8778 (2022).
- Wilson, N. P., Yao, W., Shan, J. & Xu, X. Excitons and emergent quantum phenomena in stacked 2d semiconductors. *Nature* **599**, 383–392 (2021).
- Bae, Y. J. et al. Exciton-coupled coherent magnons in a 2d semiconductor. *Nature* **609**, 282–286 (2022).
- Hou, J. et al. Unveiling the localized exciton-based photoluminescence of manganese doped cesium zinc halide nanocrystals. *Nano Lett.* **23**, 3762–3768 (2023).
- Diederich, G. M. et al. Tunable interaction between excitons and hybridized magnons in a layered semiconductor. *Nat. Nanotechnol.* **18**, 23–28 (2023).
- Zur, Y. et al. Magnetic imaging and domain nucleation in CrSBr down to the 2d limit. *Adv. Mater.* **35**, 2307195 (2023).
- Ziebel, M. E. et al. CrSBr: an air-stable, two-dimensional magnetic semiconductor. *Nano Lett.* **24**, 4319–4329 (2024).
- Alapatt, V. et al. Highly polarized single photon emitter from intrinsic localized excitons in a $\text{WSe}_2/\text{CrSBr}$ heterostructure. Preprint at <https://arxiv.org/abs/2409.04749v1> (2024).
- Rivero-Carracedo, G., Rybakov, A. & Baldoví, J. J. Magnon sensing of NO , NO_2 and NH_3 gas capture on CrSBr monolayer. *Chem. Eur. J.* e202401092 (2024).

34. Komar, R. et al. Colossal magneto-excitonic effects in 2d van der Waals magnetic semiconductor CrSBr. Preprint at <https://arxiv.org/abs/2409.00187v2> (2024).
35. Marques-Moros, F., Boix-Constant, C., Mañas-Valero, S., Canet-Ferrer, J. & Coronado, E. Interplay between optical emission and magnetism in the van der Waals magnetic semiconductor CrSBr in the two-dimensional limit. *ACS Nano* **17**, 13224–13231 (2023).
36. Telford, E. J. et al. Designing magnetic properties in CrSBr through hydrostatic pressure and ligand substitution. *Adv. Phys. Res.* **2**, 2300036 (2023).
37. Bykov, M. et al. High-pressure behavior of FeOCl. *Phys. Rev. B* **88**, 014110 (2013).
38. Bykov, M. et al. Pressure-induced normal-incommensurate and incommensurate-commensurate phase transitions in CrOCl. *Sci. Rep.* **5**, 9647 (2015).
39. Fausti, D. et al. Symmetry disquisition on the TiOX phase diagram (X = Br, Cl). *Phys. Rev. B* **75**, 245114 (2007).
40. Burch, K. S., Mandrus, D. & Park, J.-G. Magnetism in two-dimensional van der Waals materials. *Nature* **563**, 47–52 (2018).
41. Henríquez-Guerra, E. et al. Strain Engineering of Magnetoresistance and Magnetic Anisotropy in CrSBr. Preprint at <https://arxiv.org/abs/2504.09920> (2025).
42. Torres, K. et al. Probing defects and spin-phonon coupling in CrSBr via resonant Raman scattering. *Adv. Funct. Mater.* **33**, 2211366 (2023).
43. Pawbake, A. et al. Raman scattering signatures of strong spin-phonon coupling in the bulk magnetic van der Waals material CrSBr. *Phys. Rev. B* **107**, 075421 (2023).
44. Zhang, T. et al. Magnetism and optical anisotropy in van der Waals antiferromagnetic insulator CrOCl. *ACS Nano* **13**, 11353–11362 (2019).
45. Gu, Y. et al. Phonon mixing in the charge density wave state of ScV₆Sn₆. *npj Quantum Mater.* **8**, 58 (2023).
46. Krantz, M., Thomsen, C. & Cardona, M. et al. Raman-active phonons and mode softening in superconducting HgBa₂CuO_{4+δ}. *Phys. Rev. B* **50**, 1165 (1994).
47. Lukačević, I., Gupta, S. K., Jha, P. K. & Kirin, D. Lattice dynamics and Raman spectrum of rutile TiO₂: The role of soft phonon modes in pressure induced phase transition. *Mater. Chem. Phys.* **137**, 282–289 (2012).
48. Susmitha, B., Arjun, K. & Karthikeyan, B. Raman spectral studies on phonon softening, surface temperature, fano resonance, and phase change in MoS₂ nanoflakes. *Appl. Phys. A* **129**, 309 (2023).
49. Kroumova, E. et al. Bilbao crystallographic server: useful databases and tools for phase-transition studies. *Phase Transit.* **76**, 155–170 (2003).
50. Fan, S. et al. Vibrational fingerprints of ferroelectric HfO₂. *npj Quantum Mater.* **7**, 32 (2022).
51. Musfeldt, J. et al. Structural phase purification of bulk HfO₂:Y through pressure cycling. *Proc. Natl. Acad. Sci. USA* **121**, e2312571121 (2024).
52. Zhang, J. et al. Magnetoelastic coupling in the incommensurate antiferromagnetic phase of FeOCl. *Phys. Rev. B Condens. Matter Mater. Phys.* **86**, 134428 (2012).
53. Walsh, J. P. & Freedman, D. E. High-pressure synthesis: a new frontier in the search for next-generation intermetallic compounds. *Acc. Chem. Res.* **51**, 1315–1323 (2018).
54. Klein, R. et al. High-pressure synthesis of the BiVO₃ perovskite. *Phys. Rev. Mater.* **3**, 064411 (2019).
55. Müller, C. J., Schwarz, U., Schmidt, P., Schnelle, W. & Doert, T. High-pressure synthesis, crystal structure, and properties of GdS₂ with thermodynamic investigations in the phase diagram Gd-S. *Z. Anorg. Allg. Chem.* **636**, 947–953 (2010).
56. Rybakov, A. et al. Probing short-range correlations in the van der Waals Magnet CrSBr by small-angle neutron scattering. *Small Sci.* **4**, 2400244 (2024).
57. Boix-Constant, C. et al. Programmable magnetic hysteresis in orthogonally-twisted 2D CrSBr magnets via stacking engineering. *Adv. Mater.* **37**, 2415774 (2025).
58. Jayaraman, A. Diamond anvil cell and high-pressure physical investigations. *Rev. Mod. Phys.* **55**, 65 (1983).
59. Mao, H. K., Xu, J. & Bell, P. M. Calibration of the ruby pressure gauge to 800 kbar under quasi-hydrostatic conditions. *J. Geophys. Res. Solid Earth.* **91**, 4673–4676 (1986).
60. Aroyo, M. I. et al. Crystallography online: Bilbao crystallographic server. *Bulg. Chem. Commun.* **43**, 183–197 (2011).
61. Aroyo, M. I. et al. Bilbao crystallographic server: I. Databases and crystallographic computing programs. *Z. Kristallogr. Cryst. Mater.* **221**, 15–27 (2006).
62. Aroyo, M. I., Kirov, A., Capillas, C., Perez-Mato, J. & Wondratschek, H. Bilbao crystallographic server. ii. representations of crystallographic point groups and space groups. *Acta Crystallogr. Sect. A* **62**, 115–128 (2006).
63. Harms, N. C. et al. Symmetry progression and possible polar metallicity in NiPS₃ under pressure. *npj 2D Mater. Appl.* **6**, 40 (2022).
64. Giannozzi, P. et al. Quantum espresso: a modular and open-source software project for quantum simulations of materials. *J. Phys. Condens. Matter.* **21**, 395502 (2009).
65. Perdew, J. P., Burke, K. & Ernzerhof, M. Generalized gradient approximation made simple. *Phys. Rev. Lett.* **77**, 3865 (1996).
66. Monkhorst, H. J. & Pack, J. D. Special points for Brillouin-zone integrations. *Phys. Rev. B* **13**, 5188 (1976).
67. Togo, A. & Tanaka, I. First principles phonon calculations in materials science. *Scr. Mater.* **108**, 1–5 (2015).

Acknowledgements

J.L.M. thanks Physical Behavior of Materials, Basic Energy Sciences, U.S. Department of Energy (Contract number DE-SC0023144) for support of this research. Work at the National Synchrotron Light Source II at Brookhaven National Laboratory is funded by the Department of Energy (DE-AC98-06CH10886). Use of the 22-IR-1 beamline is supported by the National Science Foundation Division of Earth Sciences (EAR) SEES: Synchrotron Earth and Environmental Science (EAR-2223273) and Chicago/DOE Alliance Center (CDAC) DENA-0004153. We thank Y. Gu and K. A. Smith for valuable conversations. J.J.B. acknowledges the European Union (ERC2021-StG-101042680 2D-SMARTIES) and the Generalitat Valenciana (grant CIDEXG/2023/1). A.M.R. thanks the Spanish MIU (Grant No FPU21/04195). The authors in Valencia acknowledge the financial support from the Spanish MICIU (Excellence Unit “María de Maeztu” CEX2024-001467-M/AEI/10.13039/501100011033) and the Generalitat Valenciana (PROMETEO Program and a Ph.D fellowship to C.B.-C.). This study forms part of the Advanced Materials program and was supported by MCIN with funding from European Union NextGenerationEU (PRTR-C17.I1) and by the Generalitat Valencia.

Author contributions

L.J.L. and J.L.M. designed the study. C.B.C. and S.M.V. grew the crystals with guidance from E.C. L.J.L., J.L.M., and Z.L. performed the high-pressure synchrotron infrared and Raman scattering spectroscopies. A.M.R. carried out the theoretical calculations supervised by J.J.B. L.J.L. analyzed the spectral data with guidance from J.L.M. C.B., S.M., and E.C. grew the crystals. L.J.L. and J.L.M. wrote the manuscript. All authors commented on the text.

Competing interests

The authors declare no competing interests.

Additional information

Supplementary information The online version contains supplementary material available at <https://doi.org/10.1038/s41535-025-00767-2>.

Correspondence and requests for materials should be addressed to Janice L. Musfeldt.

Reprints and permissions information is available at <http://www.nature.com/reprints>

Publisher's note Springer Nature remains neutral with regard to jurisdictional claims in published maps and institutional affiliations.

Open Access This article is licensed under a Creative Commons Attribution-NonCommercial-NoDerivatives 4.0 International License, which permits any non-commercial use, sharing, distribution and reproduction in any medium or format, as long as you give appropriate credit to the original author(s) and the source, provide a link to the Creative Commons licence, and indicate if you modified the licensed material. You do not have permission under this licence to share adapted material derived from this article or parts of it. The images or other third party material in this article are included in the article's Creative Commons licence, unless indicated otherwise in a credit line to the material. If material is not included in the article's Creative Commons licence and your intended use is not permitted by statutory regulation or exceeds the permitted use, you will need to obtain permission directly from the copyright holder. To view a copy of this licence, visit <http://creativecommons.org/licenses/by-nc-nd/4.0/>.

© The Author(s) 2025